

In silico study of the posture-dependent cardiovascular performance during parabolic flights

*Original*

In silico study of the posture-dependent cardiovascular performance during parabolic flights / Fois, M., Ridolfi, L., Scarsoglio, S.. - In: ACTA ASTRONAUTICA. - ISSN 1879-2030. - ELETTRONICO. - 200:(2022), pp. 435-447. [10.1016/j.actaastro.2022.08.018]

*Availability:*

This version is available at: 11583/2971073 since: 2022-09-07T14:43:10Z

*Publisher:*

Elsevier

*Published*

DOI:10.1016/j.actaastro.2022.08.018

*Terms of use:*

This article is made available under terms and conditions as specified in the corresponding bibliographic description in the repository

*Publisher copyright*

Elsevier postprint/Author's Accepted Manuscript

© 2022. This manuscript version is made available under the CC-BY-NC-ND 4.0 license  
<http://creativecommons.org/licenses/by-nc-nd/4.0/>. The final authenticated version is available online at:  
<http://dx.doi.org/10.1016/j.actaastro.2022.08.018>

(Article begins on next page)

# *In silico* study of the posture-dependent cardiovascular performance during parabolic flights

Matteo Fois<sup>a,\*</sup>, Luca Ridolfi<sup>b</sup>, Stefania Scarsoglio<sup>a</sup>

<sup>a</sup>*Department of Mechanical and Aerospace Engineering, Politecnico di Torino, Corso Duca degli Abruzzi 24, Turin (10129), Italy*

<sup>b</sup>*Department of Environmental, Land and Infrastructure Engineering, Politecnico di Torino, Corso Duca degli Abruzzi 24, Turin (10129), Italy*

---

## Abstract

Space exploration plays a crucial role in research and technological advance. Yet, weightlessness entails severe risks for human life that are investigated through both Earth-based and on-orbit experiments. To this aim, parabolic flights are used to study the short-term response of the human cardiovascular system (*CVS*) to micro- ( $\sim 0g$ ) and hypergravity (up to 1.8g). However, the short flight duration and technical difficulties associated with invasive *in vivo* measurements allow for the acquisition of a very limited number of hemodynamic variables. To enrich the picture, numerical tools can represent a powerful alternative. In this work, a new validated multiscale model of the *CVS* is proposed to inquire into global and central hemodynamic alterations - including cardiac mechano-energetic balance - triggered by parabolic flight at different postures (supine, seated and standing). Our analyses show that: (i) gravity-induced *CVS* changes strongly depend on posture; (ii) central aortic pressure, cardiac work and oxygen consumption indexes are significantly influenced by blood migration between central and lower body regions elicited by gravity variation; and (iii) cardiac efficiency improves during 20 s microgravity, while worsening in both hypergravity phases. Finally, (iv) the role of mildly elevated intracranial pressure (*ICP*) encountered in 0g is discussed as a potential risk factor for spaceflight-induced visual impairment.

*Keywords:* computational hemodynamics, multiscale cardiovascular modeling, parabolic flight, bioastronautics, cardiac performance, intracranial pressure

---

## 1. Introduction

Spaceflights and interplanetary explorations have always aroused enormous fascination and interest in mankind, and in recent decades they are becoming more and more accessible. Unfortunately, still little is known concerning human adaptation to the space environment, although multiple risks and life-threatening consequences (*i.e.*, bone mass loss, osteoporosis, radiation exposure, muscular atrophy) have been revealed by recent studies for missions lasting up to six

---

\*Corresponding author

7 months [1–5]. Among different ground analogs of microgravity conditions (head-down tilt, water  
8 immersion, drop towers, etc. [3]), parabolic flights are the only ones where actual free-falling -  
9 albeit of limited duration - is reproduced on passengers. This is possible due to the almost com-  
10 plete body gravity unloading experienced at the apex of the parabolic trajectory followed during  
11 a parabolic flight, which is performed 20-30 times for each experimental campaign. Differently,  
12 water immersion and head-down bed rest produce only virtual gravity unloading, either by align-  
13 ing the body axis perpendicularly to the gravity vector, or due to the pulling action exerted by  
14 the liquid, whereas drop towers experiments are definitely unfeasible. Therefore, parabolic flights  
15 represent the cheapest and most affordable Earth analog of actual spaceflight in mimicking short-  
16 term microgravity occurrence on humans. For each parabola, the subjects undergo a sequence of  
17 short-term exposure to hypergravity (after the pull-up from 1g to 1.8g), followed by microgravity  
18 ( $\sim 0g$ ) and a second hypergravity (with subsequent pull-out from 1.8g to 1g) phases, lasting about  
19 20 s each, including transitions. Therefore, the spurious influence of the pre- and post-0g hyper-  
20 gravity phases should be taken into consideration when analyzing the subjects response to acute  
21 microgravity.

22 In past years, a conspicuous number of parabolic flight campaigns were promoted with the  
23 purpose of collecting information about the human physiological systems coping with reduced  
24 gravity. In particular, the role of the cardiovascular system ( $CVS^1$ ) was explored, even though  
25 only simple and, in most cases, non-invasive *in vivo* measurements were acquired (*e.g.*, heart rate,  
26 finger or brachial arterial pressure). Most authors focused on single phase-averaged responses  
27 of main hemodynamic variables [6–11], though some reported also continuous monitoring of the  
28 investigated parameters [12–14]. In [6], the authors provided a detailed analysis on the role of  
29 posture in the hemodynamic response to parabolic flight, whereas in other works different aspects  
30 were explored, such as post-flight induced orthostatic intolerance [15], the impact of the Valsalva  
31 maneuver [16] or the particular response to different reduced-gravity environments (*e.g.*, Moon,  
32 Mars) [17, 18]. Only few studies [14, 19] reported data from (non-invasive) estimation of central  
33 aortic pressure, obtained by transfer function reconstruction. Yet, comprehension of central (aortic  
34 and cardiac) hemodynamics is crucial to adequately assess the actual  $CVS$  response to weightless-  
35 ness. For instance, catheterized monitoring of central venous pressure ( $CVP$ ) during a parabolic  
36 flight campaign showed fundamental discrepancies with respect to other ground experiments often  
37 considered as analogs of microgravity conditions, such as head-down bed rest studies [20].

38 In this perspective, numerical modeling has recently proved very effective to investigate the  
39 hemodynamic behavior and the  $CVS$  response induced by gravity changes [21–24]. In spite of such,  
40 to the best of our knowledge, the only attempts to numerically reproduce parabolic flight effects  
41 onto  $CVS$  were carried out by Gerber *et al.* [25], who performed simulations of gravity acceleration  
42 variation from 1g to 1.8g and then to 0g on a lumped parameter model of the circulation, though

---

<sup>1</sup>See Nomenclature at end of paper

43 assuming fictitious time transitions to stabilize the model.

44 To fully exploit the potentialities of the computational approach, in the present study we adopt  
45 the multiscale 1D-0D mathematical model of the human *CVS* proposed in our recent work [21] to  
46 simulate the posture-depending hemodynamic response to gravity changes induced by parabolic  
47 flight. Based on this recent study on the role of body tilting onto the *CVS* response, we can specu-  
48 late that the *CVS* response to gravity increase (from 0g to 1g and then to 1.8g) in standing posture  
49 will likely follow a similar direction to that observed when tilting from supine to upright standing.  
50 The analysis is carried out during all phases (1g - 1.8g - 0g - 1.8g - 1g) and postures (supine,  
51 seated and standing) typically encountered during a conventional parabolic flight. The model  
52 encompasses a 1D description of the coronary and arterial tree along with a lumped parameter-  
53 ization of the venous return, peripheral microcirculation and cardiopulmonary circulation. The  
54 lumped systemic compartments are organized into distinct regions (from head to legs) to account  
55 for the heterogeneous effect of gravity throughout the body. The model incorporates short-term  
56 regulation mechanisms of blood pressure (arterial baroreflex and cardiopulmonary reflex) and flow  
57 (cerebral autoregulation), aimed at controlling the heart rate, cardiac contractility, peripheral  
58 vasodilation/constriction and venous tone. A suitable pressure-area relationship [26] is included  
59 for 1D carotid and vertebral arteries to deal with very low transmural pressures elicited during  
60 1.8g flight phases [27–29]. Intracranial pressure (*ICP*) variation with posture and gravity is also  
61 modeled to mimic cerebrospinal fluid interplay with cerebral vessels. In addition, a model for  
62 intrathoracic pressure (*ITP*) variation with body posture and gravity acceleration is enclosed  
63 to account for thoracic cavity compression and relaxation and their relevant effect onto central  
64 hemodynamics experienced during parabolic flights [5, 30].

65 The aims of our analysis are: (i) to test the model outcomes with the most common hemody-  
66 namic parameters found in the literature; (ii) to study the dynamics of some crucial parameters  
67 - such as central aortic pressure behavior - not generally observed during parabolic flights due to  
68 their difficult measurement (*e.g.*, through catheterization); and (iii) to assess the transient cardiac  
69 mechano-energetic response. Finally, (iv) we discuss the role of microgravity-induced elevated *ICP*  
70 as plausible hemodynamic mechanism inducing long-term spaceflight visual impairment.

## 71 **2. Material and Methods**

### 72 *2.1. The CVS model*

73 The multiscale model of the human circulation adopted in this work was developed and vali-  
74 dated in our previous study on *CVS* response to posture changes [21]. The model architecture -  
75 displayed in Figure 1 - encompasses a 1D description of the arterial tree (aorta plus large systemic  
76 and coronary arteries) linked to 0D analogs of the systemic peripheral microcirculation (arteriolar,  
77 capillary and venular) and the venous return (veins and venae cavae), organized into five separate

78 body regions, from head to legs, as illustrated in the right panel of Figure 1. The model equations  
79 and parameters definition are reported in the Supplementary Material.

80 Blood motion through 1D arteries is governed by the axisymmetric form of the Navier-Stokes  
81 equations, by assuming a flat-parabolic longitudinal velocity profile over each vessel cross-section  
82 area (details in [31]). The gravity contribution is enclosed as external forcing field within the  
83 momentum balance. A non-linear viscoelastic constitutive equation for blood pressure is included  
84 to account for arterial walls mechanical properties. Mass and total pressure conservation are  
85 imposed at arterial bifurcations, while a set of lumped characteristic impedances link each terminal  
86 1D artery with the following 0D arterioles. The 1D aorta is directly connected to the 0D left  
87 ventricle through a lumped aortic valve model. Specific numerical boundary conditions are derived  
88 for the aorta-left ventricle coupling, at bifurcations and at each terminal artery outlet section  
89 through the method of characteristics [31]. 1D governing equations were discretized and solved  
90 numerically according to a Discontinuous Galerkin Finite Elements approach, and integrated in  
91 time employing a 2-step Runge-Kutta explicit scheme with constant time step (details in [21]).

92 The 0D circuital RLC compartments are modeled as a system of ordinary differential equa-  
93 tions for mass and momentum balance, accounting for vessels hydraulic resistance ( $R$ ) and blood  
94 inertia ( $L$ ), and by a linear algebraic constitutive equation for blood pressure depending on vessels  
95 compliance ( $C$ ). Gravity is introduced via pressure sources within extended venous compartments  
96 (*i.e.*, head, arms, legs and venae cavae) according to Stevino's law, while a specific non-linear  
97 pressure-volume relationship (Melchior *et al.* [32]) is introduced to deal with posture-induced ele-  
98 vated transmural pressures encountered in leg veins (as indicated by brown squares in Figure 1).  
99 Arms and legs venous compartments are further equipped with a lumped model of venous valves,  
100 to prevent from reverse flow. Head veins are subjected to the action of extravascular intracranial  
101 pressure ( $ICP$  in Figure 1), due to cerebrospinal fluid pressure, which is modulated with posture  
102 so that head veins transmural pressure remains negligible (details on  $ICP$  model implementation  
103 are addressed in Appendix A).

104 The 0D analog of the cardiopulmonary circulation includes a time-varying elastance and a  
105 valve model for each cardiac chamber, along with lumped pulmonary arteries and veins RC com-  
106 partments, as illustrated in Figure 1. All cardiopulmonary compartments are subjected to the  
107 action of extravascular/extrachamber intrathoracic pressure ( $ITP$  in Figure 1), which varies with  
108 posture and gravity acceleration, inducing marked changes in cardiac filling and central venous  
109 pressure ( $CVP$ , that is the right atrial pressure). The multiscale model of the coronary circulation  
110 corresponds to the one developed by Mynard & Smolich [33]. The 0D analog of the coronary  
111 microvasculature describes the perfusion of the different myocardial layers, primarily driven by  
112 the action of extravascular intramyocardial pressure ( $IMP$  in Figure 1). Further details on the  
113 coronary vasculature modeling are reported in [34].

114 The model includes short-term blood pressure and flow control aimed at maintaining the system  
115 homeostasis. In particular, an arterial baroreflex model is implemented - with target pressure the

116 steady-state supine mean aortic-carotid pressure - controlling the heart chronotropic and inotropic  
117 effects, arteriolar and capillary vasodilation/constriction and venous tone (venular and venous un-  
118 stressed volumes and compliances). The cardiopulmonary reflex is also enclosed, targeting the  
119 mean supine right atrial pressure (*i.e.*, *CVP*), and controlling peripheral resistances and venous  
120 tone as well. Then, a cerebral autoregulation model is added to maintain proper perfusion of brain  
121 tissues during the various phases of the parabolic flight. The cerebral autoregulation model was al-  
122 ready present in our previous work on posture changes [21], and was included in the present study  
123 since a mechanism regulating cerebral blood flow has been proved to hold also during parabolic  
124 flight [14, 35]. In the present work, to resemble typical pre-flight conditions commonly observed in  
125 parabolic flight experiments [6–19], the saturation parameters of arterial baroreflex and cardiopul-  
126 monary reflex are slightly modified with respect to passive tilting condition [21] - with new settings  
127 reported in Supplementary Table 1 of the Supplementary Material - meanwhile keeping unaltered  
128 all the parameters associated with cerebral autoregulation. The improved response of short-term  
129 regulation control can be ascribed to the challenging and not completely passive pre-flight condi-  
130 tion, where complete absence of muscular activation and bio-chemical factors intervention cannot  
131 be excluded *a priori*. All ordinary differential equations governing 0D compartments and regula-  
132 tion mechanisms were integrated in time via the same 2-step Runge-Kutta explicit scheme applied  
133 to the 1D discretized governing equations (details in [21]).

134 To further align with typical pre-flight conditions commonly observed in parabolic flight ex-  
135 periments [6–19], hydraulic resistances associated with arteriolar compartments are increased by  
136 15% with respect to [21]. In the following sub-sections, only the new modeling aspects *ad hoc* in-  
137 troduced to account for parabolic flight effects are presented, while the remaining components and  
138 settings of the model (including related numerical algorithms) remain as reported in our previous  
139 work [21].

### 140 2.1.1. Pressure-Area relationship for carotid and vertebral 1D arteries

141 The hypergravity phase (about 1.8g) of a parabolic flight elicits strong changes in the *CVS*,  
142 especially at seated and standing postures. Iwasaki *et al.* [27] showed that carotid mean arterial  
143 pressure can drop below 45 mmHg at 1.5g along the longitudinal body axis, although only partial  
144 constriction of the carotid arteries occurs [28]. Linnarsson *et al.* [29] proved that such carotid  
145 arterial pressure drop was present even at higher ventricular rate, during exercise.

146 The constitutive pressure-area ( $p$ - $A$ ) relationship describing arterial walls mechanics incorpo-  
147 rated in our *CVS* model [21] was developed by Guala *et al.* [31], and was validated within the  
148 range 50-120 mmHg. To deal with very low arterial pressure encountered at terminal carotid and  
149 vertebral arteries, the model by Guala *et al.* was extended by introducing the partial collapse  
150 hyperbolic relationship proposed by Drzewiecki *et al.* [26], so that the novel  $p$ - $A$  relationship  
151 reads

$$152 \quad p = B_1 + B_2A + B_3A^2 + B_4A^3 - B_5 \frac{1}{\sqrt{A}} \frac{\partial Q}{\partial x} - \widehat{EI} \left( \left( \frac{A_b}{A} \right)^n - 1 \right) + p_b, \quad (1)$$

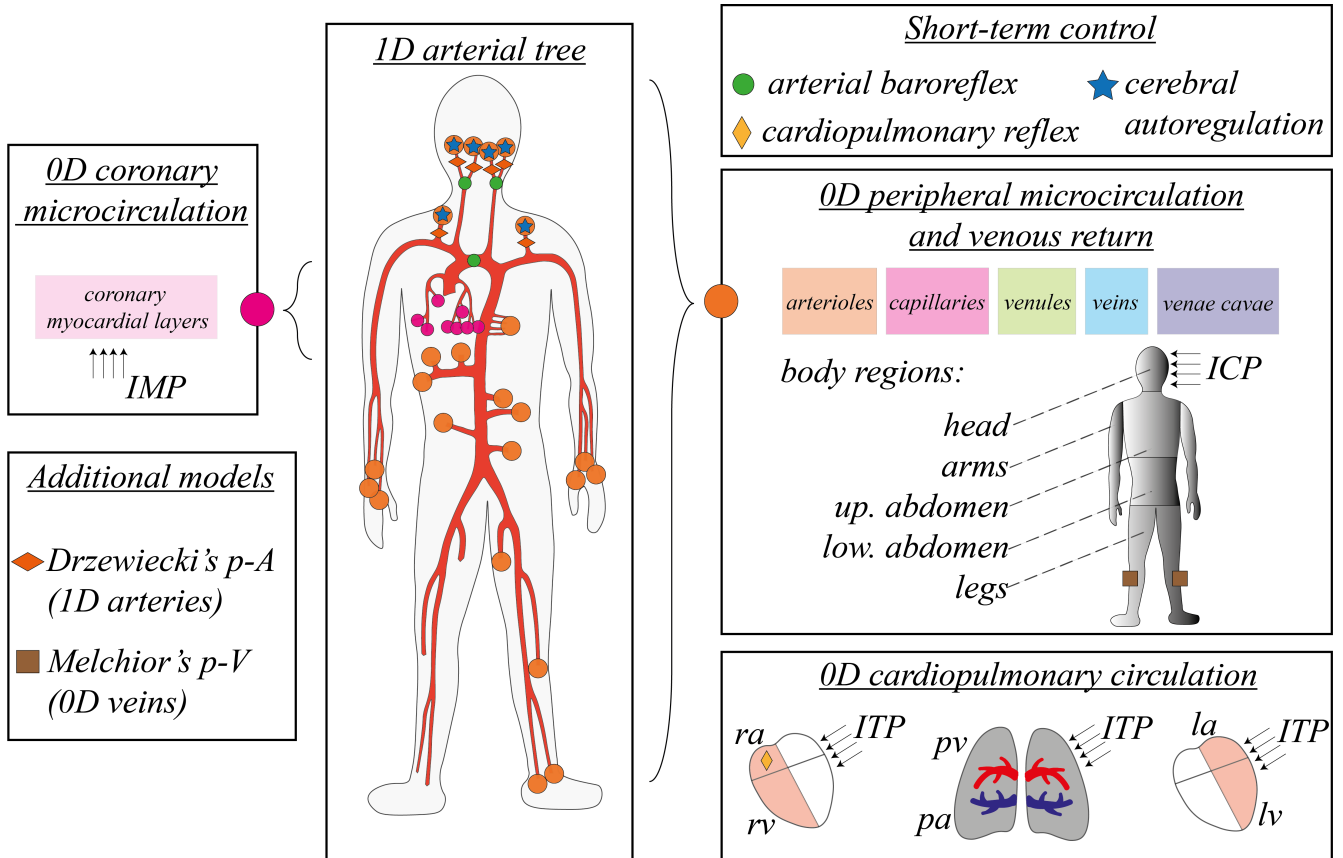


Figure 1: schematic illustration of the global multiscale *CVS* model (details in [21]). The red network represents 1D arteries, while the colored bands in the right panel (orange, pink, green and blue, from left to right) refer to the different compartments of the 0D systemic circulation (from arterioles to venae cavae, respectively). Orange circles indicate 1D arterial connections with distal 0D arterioles, organized by different body region (from head to legs). The 0D cardiopulmonary circulation is depicted in the bottom right panel, where *ra* and *rv* are right atrium and ventricle, *pa* and *pv* are pulmonary arteries and veins, whereas *la* and *lv* are left atrium and ventricle, respectively. The 1D coronary circulation is linked to its 0D microcirculation analog through violet circles (details in [34]). *IMP*, *ICP*, and *ITP* are intramyocardial, intracranial and intrathoracic pressures, while *p-A* and *p-V* denote vessels pressure-area and pressure-volume relationships, respectively.

Table 1: assumed value of intrathoracic pressure (*ITP*) depending on body posture (supine or seated/standing) and gravity acceleration  $g/g_0$  (values from [5, 20, 30]).

Intrathoracic pressure <i>ITP</i> [mmHg]			
	0g	1g	1.8g
supine	-4.1	-2.5	-2.2
seated	-4.1	-6.5	-7.2
standing	-4.1	-6.5	-7.2

153 where  $p = p(x, t)$  is arterial transmural pressure ( $t$  is time and  $x$  is vessels axial coordinate),  
 154  $A = A(x, t)$  is vessel cross-section area,  $Q = Q(x, t)$  is blood flow rate, and coefficients  $B_i = B_i(x)$   
 155 ( $i = 1 \dots 5$ ) depend on vessels mechanical properties. The remaining terms represent Drzewiecki's  
 156 partial collapse model, where  $\widehat{EI} = 4.14$  mmHg is the vessel flexural rigidity normalized by the  
 157 lumen radius cubed,  $A_b = 10$  mm<sup>2</sup> and  $p_b = -0.64$  mmHg are buckling cross-section area and  
 158 pressure (at maximum compliance), respectively, while  $n = 2$  is a constant defining the degree of  
 159 curvature of the  $p$ - $A$  hyperbola. Eq. (1) applies to carotid and vertebral arteries as indicated by  
 160 orange rhombs in Figure 1.

### 161 2.1.2. Intrathoracic pressure vs. posture and gravity acceleration

162 Beside physiological *ITP* variation with body posture [21], Peterson *et al.* [30] highlighted that  
 163 intrathoracic pressure is differently affected by gravity acceleration whether the subject lies supine  
 164 or stands upright, due to the pushing action of the diaphragm against the thoracic cavity, as also  
 165 confirmed by Norsk [5] and Videbaek & Norsk [20]. In supine posture, the diaphragm is pushed  
 166 headward by the compression of the abdominal cavity with increasing gravity, thus raising *ITP*  
 167 inside the thoracic cavity. Conversely, at seated or standing posture, an augmented gravity results  
 168 in a releasing effect onto the thoracic cavity (*i.e.*, lower *ITP*) by pulling the diaphragm feetwards.

169  
 170 To take into account this diaphragm-induced effect onto the thoracic cavity state, we propose  
 171 a novel *ITP* model as a function of posture (through the tilt angle  $\alpha$ ) and gravity acceleration  
 172 (normalized as  $g/g_0$ , where  $g_0=9.81$  m/s<sup>2</sup>) by fitting data recorded in previous works (see Table 1).  
 173 The new *ITP* model reads

$$174 \quad ITP = -4.014 + 1.127 \frac{g}{g_0} + 0.895 \left( \frac{g}{g_0} \right)^2 \sin(\alpha) - 4.508 \frac{g}{g_0} \sin(\alpha), \quad (2)$$

175 with standard squared error  $SSE = 0.21$  mmHg<sup>2</sup> and coefficient of determination  $R^2 = 0.99$ . The  
 176 *ITP* time profiles computed through eq. (2) along the parabolic flight trajectory at varying  $g/g_0$   
 177 for both supine and seated/standing postures are reported in Figure 2.

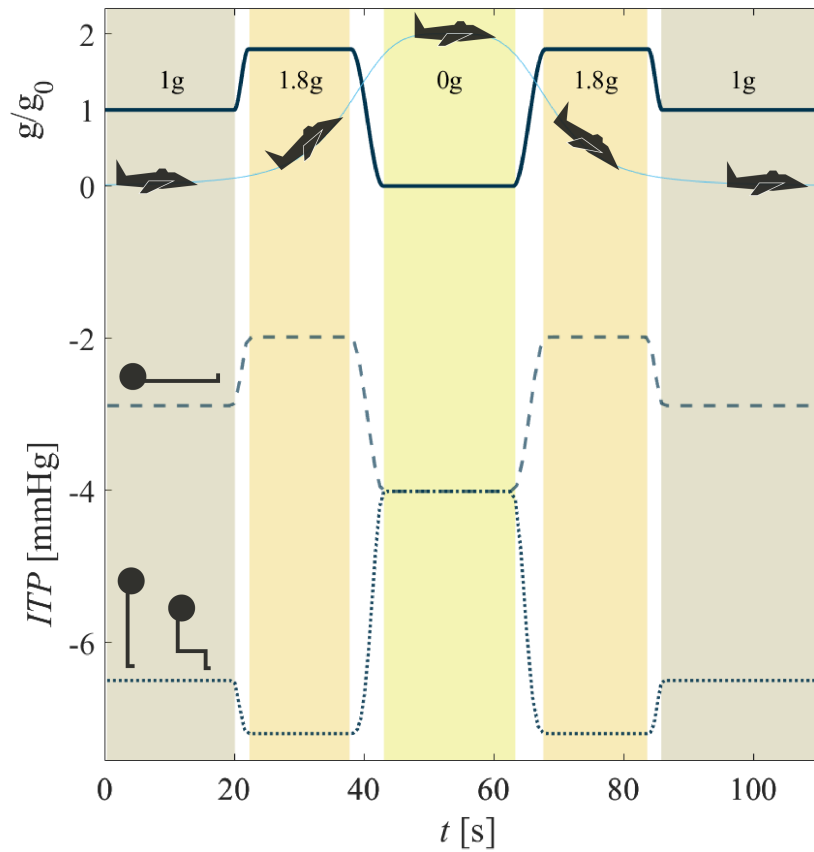


Figure 2: illustration of the parabolic flight time profile. On top, the parabolic flight profile is sketched together with the corresponding gravity acceleration profile  $g/g_0$  (with  $g_0 = 9.81 \text{ m/s}^2$ ). Below, the time behavior of intrathoracic pressure  $ITP$  at different postures (supine: dashed line; seated and standing: dotted line) is reported.

178 *2.2. Baseline postures*

179 To comply with standard pre-flight measurements collected from the literature [6–19] and  
 180 to allow for comparisons among different cardiovascular responses during the parabolic flight  
 181 maneuver, baseline (pre-flight) supine, seated and standing postures are introduced. These three  
 182 different pre-flight configurations (adopted as initial conditions for the parabolic flight simulations)  
 183 are defined by exploiting the steady-state *CVS* configuration approached after simulated passive  
 184 head-up tilt to 90° performed as described in [21] (no tilting is performed for the supine posture),  
 185 assuming the new model calibration introduced in section 2.1.

186 In particular, the pre-flight baseline seated posture is obtained by simulating tilt from supine  
 187 to upright 90° via the following assumptions: (i) at  $\alpha \neq 0$  the gravitational contribution to  
 188 the momentum balance equation is neglected along the whole femoral and deep femoral arteries  
 189 (arteries #45 and #46 with reference to [21]); (ii) the hydrostatic height of the 0D legs venous  
 190 compartment is reduced by accounting for only half the anatomical length of the leg veins.

191 *2.3. Parabolic flight simulation*

192 A standard parabolic flight profile is designed on the basis of the most common parabolic flight  
 193 campaigns reported in the literature [6–19]. Typically, the duration of each phase of flight (hyper-  
 194 and microgravity) lasts about 20 s, with fast transitions between each phase of few seconds (refer  
 195 to the flight profiles reported by Mukai *et al.* [6] and Liu *et al.* [12]). The implemented  $g/g_0$   
 196 time profile is depicted in Figure 2, together with the corresponding sketch of the parabolic flight  
 197 trajectory. Each gravity transition is modeled as a cosinusoidal function of time:

$$198 \quad \frac{g}{g_0} = \left( \frac{g}{g_0} \right)_i \pm \frac{1}{2} \left[ \left( \frac{g}{g_0} \right)_f - \left( \frac{g}{g_0} \right)_i \right] \cdot \left[ 1 \mp \cos \left( \frac{t - t_i}{\Delta t_{i-f}} \pi \right) \right], \quad (3)$$

199 taking the upper sign for ascending  $g/g_0$  ramps, whereas the lower one for descending  $g/g_0$  ramps.  
 200 In eq. (3), subscripts  $i$  and  $f$  refer to the initial and final gravity acceleration magnitude of the  
 201 corresponding transition phases, respectively, with  $t_i$  and  $\Delta t_{if}$  being the starting time of transition  
 202 and the transition phase duration, respectively. Both the pull-up (1g-1.8g) and pull-out (1.8g-1g)  
 203 phases as well as the parabolic maneuver (1.8g-0g and subsequent 0g-1.8g) are performed at  
 204 fixed time rate ( $\pm 0.36$  g/s). The duration of each gravity transition phase  $\Delta t_{i-f}$  (*i.e.*,  $\Delta t_{1g-1.8g}$ ,  
 205  $\Delta t_{1.8g-0g}$  and *vice versa*) is reported in Table 2, together with the time duration of each phase of  
 206 flight:  $T_{1.8g}^I$  and  $T_{1.8g}^{II}$  for the first and second hypergravity phases, and  $T_{0g}$  for the microgravity  
 207 phase, respectively.

208 *2.4. Mechano-energetic indexes*

209 To grasp information regarding the global *CVS* mechano-energetic balance (*i.e.*, the cardiac  
 210 oxygen demand-supply ratio) during parabolic flight, we focus on the behavior of the different  
 211 oxygen consumption indexes - the rate-pressure product *RPP*, the tension-time index *TTI* and

Table 2: assumed values for the  $g/g_0$  time profile parameters of a conventional parabolic flight.  $\Delta t_{1g-1.8g}$ ,  $\Delta t_{1.8g-0g}$ ,  $\Delta t_{0g-1.8g}$ ,  $\Delta t_{1.8g-1g}$  are the gravity transitions duration from 1g to 1.8g, from 1.8g to 0g, from 0g to 1.8g and from 1.8g to 1g, respectively, whereas  $T_{1.8g}^I$ ,  $T_{1.8g}^{II}$  and  $T_{0g}$  are the time durations of the first and second hypergravity and of the microgravity phases, respectively.

Param.	$\Delta t_{1g-1.8g}$	$T_{1.8g}^I$	$\Delta t_{1.8g-0g}$	$T_{0g}$	$\Delta t_{0g-1.8g}$	$T_{1.8g}^{II}$	$\Delta t_{1.8g-1g}$
Value [s]	2.2	15.8	5.0	20.0	5.0	15.8	2.2

212 the pressure-volume area  $PVA$  [36] - and the corresponding energy supply parameter, described  
 213 by the cardiac work (or stroke work,  $SW$ ), corresponding to the area of the left ventricle pressure-  
 214 volume loop. The analyzed beat-to-beat oxygen consumption indexes are defined as:

$$215 \quad RPP = p_{aor,sys} \cdot HR, \quad (4)$$

216 where  $p_{aor,sys}$  is aortic systolic pressure;

$$217 \quad TTI = p_{lv,mean} \cdot RR, \quad (5)$$

218 with  $p_{lv,mean}$  being the mean left ventricle pressure computed over the heartbeat, while  $EF$  is the  
 219 heartbeat duration; and

$$220 \quad PVA = PE + SW, \quad (6)$$

221 where  $PE$  is left ventricle potential energy, defined as  $PE = p_{lves}(V_{lves} - V_{lv}^{un})/2 - p_{lved}(V_{lved} - V_{lv}^{un})/2$ ,  
 222 with  $p_{lves}$ ,  $p_{lved}$ ,  $V_{lves}$ ,  $V_{lved}$  and  $V_{lv}^{un}$  being left ventricle end-systolic and end-diastolic pressures,  
 223 end-systolic and end-diastolic volumes, and unstressed volume, respectively.

224 We also assess cardiac efficiency by means of the ejection fraction

$$225 \quad EF = SV/V_{lved}, \quad (7)$$

226 expressing the ratio between blood volume ejected from the left ventricle ( $SV$ ) and the maximum  
 227 available left ventricular volume (end-diastolic volume,  $V_{lved}$ ), and  $SW/PVA$ , the cardiac energy  
 228 supply vs. demand ratio. To allow for the comparison between flight phases and postures, as well  
 229 as with  $RPP$ , all these quantities are expressed per minute by multiplying them by the heart  
 230 rate  $HR$  (*i.e.*,  $SW/\text{min} = SW \cdot HR$ ,  $PVA/\text{min} = PVA \cdot HR$ ,  $TTI/\text{min} = TTI \cdot HR$ ).

### 231 3. Model validation through global hemodynamic response

232 The model outcomes for the most commonly measured hemodynamic parameters over each  
 233 phase of the parabolic flight profile at supine, seated and standing postures [6–19] are reported  
 234 in Table 3. The investigated parameters include: mean, systolic and diastolic arterial pressure

235 ( $MAP$ ,  $SAP$  and  $DAP$ , respectively), heart rate ( $HR$ ), left ventricle stroke volume ( $SV$ ), cardiac  
236 output ( $CO$ ) and total peripheral resistance ( $TPR$ ). We recall that, as a standard practice during  
237 *in vivo* measurements aboard of parabolic flight campaigns, all authors reported arterial pressure  
238 measurements taken at peripheral sites - commonly at the finger through non-invasive photo-  
239 plethysmography and continuous beat-to-beat recording - with concurrent or subsequent correction  
240 at heart level, by keeping the hand at same height of the heart, or via suitable pressure correction.  
241 For this reason,  $MAP$ ,  $SAP$  and  $DAP$  in Table 3 are always referred to the model finger arterial  
242 pressure (outlet section of the 1D radial artery), with subsequent subtraction of the hydrostatic  
243 contribution associated with the vertical distance between the heart and the selected site.

244 Although most authors performed continuous non-invasive recording of arterial pressure and  
245  $HR$ , the complete time history of the inquired hemodynamic variables was made available only  
246 by a few of them [12–14, 16–18]. Furthermore, the criteria for the calculation of the single flight  
247 phase average value of a given hemodynamic parameter remains heterogeneous among the authors.  
248 Thus, following Ogoh *et al.* [14], we report the single-phase time average value of each parameter  
249 evaluated over the last 10 s of each phase of flight. This allows us to exclude the first and strongest  
250 fluctuations immediately past each gravity transition.

251 Table 3 shows that the model is capable of accurately reproducing the global hemodynamic  
252 response to parabolic flights at different postures. The largest pressure discrepancies with respect  
253 to the measured data emerge within the 1.8g phases at seated and standing postures, probably  
254 because of the shorter duration of these flight phases - making the set of measured values more  
255 heterogeneous - and due to the arterial site where the pressure signal is detected. Indeed, even  
256 though close to the finger, the radial artery does not coincide with the typical finger cuff place-  
257 ment, thus inducing unavoidable slight pressure waveform mismatches which are the cause for the  
258 observed differences between computed and measured  $MAP$ ,  $SAP$  and  $DAP$ .

259 The overall hemodynamic response is well captured also in the case of supine posture. We  
260 recall that the gravity term is introduced in our model only along the main body longitudinal axis  
261 (*i.e.*, along the head-feet direction), thus no direct alteration should occur at  $\alpha=0$  (supine). How-  
262 ever, gravity does manifest its effect through intrathoracic pressure variation (by compression or  
263 expansion of the thoracic cavity on behalf of the diaphragm), triggering weak but still appreciable  
264 hemodynamic changes. Such parameters fluctuations appear to be in the same direction as those  
265 observed in the literature [5–8, 10, 12, 13], although Bimpong-Buta *et al.* [7] and Liu *et al.* [12]  
266 were not able to prove statistical significance of their findings.

267 Compared with initial and final 1g phases, the 20 s microgravity phase shows an overall hemo-  
268 dynamic relaxation at all postures in terms of arterial pressure and cardiac performance. Moreover,  
269 supine 1g differs slightly from supine 0g, as well as from seated and standing 0g. The reason for  
270 such a mismatch is in fact the action of intrathoracic pressure: this latter approaches a similar  
271 value upon microgravity at all postures - lower than 1g in supine posture - thus causing improved  
272 venous return and subsequent enhanced ventricular filling, together with reduction of the heart

Table 3: comparison between model outcomes and measured data for the most common hemodynamic parameters divided by posture and flight phase. *MAP* mean arterial pressure, *SAP* systolic arterial pressure, *DAP* diastolic arterial pressure (blood pressures always referred to finger arterial pressure corrected at heart level), *HR* heart rate, *SV* stroke volume, *CO* cardiac output, *TPR* total peripheral resistance. The model outcomes are computed by averaging the last 10 s of each flight phase (percentage variations with respect to standing 1g values are included only when absolute ranges are not available in literature). Benchmark values are taken from [6–19] and are reported in squared brackets. Symbols help identify trends reported in the literature for the corresponding variables, with respect to their 1g pre-flight state ( $\cong$ : not clear trend,  $\uparrow$ : parameter increase,  $\downarrow$ : parameter decrease).

Posture	Parameter	1g	1.8g	0g	1.8g	1g
Supine	<i>MAP</i> [mmHg]	87 [73÷101]	85 [68÷98] $\cong$	89 [78÷96] $\cong$	84 [68÷95] $\cong$	87 [75÷95]
	<i>SAP</i> [mmHg]	150 [112÷144]	146 [113÷139] $\cong$	154 [120÷144] $\cong$	146 [111÷139] $\cong$	150 [114÷144]
	<i>DAP</i> [mmHg]	54 [55÷83]	54 [53÷81] $\cong$	54 [60÷80] $\cong$	53 [53÷75] $\cong$	54 [57÷79]
	<i>HR</i> [bpm]	70 [60÷89]	74 [60÷88] $\cong$	66 [61÷91] $\cong$	73 [61÷84] $\cong$	70 [60÷88]
	<i>SV</i> [ml]	76 (123%) [132%÷134%]	71 (115%) [126%÷142%] $\cong$	82 (133%) [125%÷151%] $\cong\uparrow$	72 (116%) [124%÷138%] $\cong$	76 (123%) [130%÷136%]
	<i>CO</i> [l/min]	5.3 (109%) [106%÷108%]	5.2 (107%) [97%÷121%] $\cong$	5.4 (111%) [98%÷122%] $\cong\uparrow$	5.2 (108%) [91%÷115%] $\cong$	5.3 (109%) [103%÷109%]
	<i>TPR</i> [mmHg·min/l]	16.1 (82%) [80%÷82%]	15.9 (81%) [70%÷90%] $\cong$	16.4 (83%) [71%÷89%] $\cong$	15.9 (80%) [77%÷87%] $\cong$	16.2 (82%) [77%÷87%]
Seated	<i>MAP</i> [mmHg]	97 [85÷105]	96 [90÷110] $\cong\downarrow$	88 [70÷101] $\downarrow$	84 [80÷105] $\cong\downarrow$	97 [80÷110]
	<i>SAP</i> [mmHg]	158 [109÷153]	151 [110÷155] $\cong\uparrow$	158 [102÷133] $\cong\downarrow$	132 [110÷156] $\cong$	158 [125÷163]
	<i>DAP</i> [mmHg]	69 [69÷89]	74 [73÷99] $\uparrow$	51 [57÷79] $\downarrow$	64 [68÷92] $\cong$	69 [71÷89]
	<i>HR</i> [bpm]	74 [63÷86]	99 [74÷113] $\uparrow$	68 [62÷90] $\downarrow$	108 [74÷109] $\uparrow$	75 [67÷93]
	<i>SV</i> [ml]	68 (110%) [50÷111]	48 (78%) [40÷90] $\downarrow$	87 (142%) [70÷125] $\uparrow$	41 (67%) [50÷100] $\downarrow$	68 (110%) [50÷100]
	<i>CO</i> [l/min]	5.0 (104%) [4.0÷8.5]	4.8 (98%) [4.0÷8.9] $\downarrow$	5.9 (122%) [5.0÷9.9] $\uparrow$	4.5 (92%) [4.5÷8.9] $\downarrow$	5.0 (104%) [4.0÷8.0]
	<i>TPR</i> [mmHg·min/l]	19.4 (98%) [11.8÷22.2]	20.1 (102%) [12.5÷25.0] $\cong\uparrow$	14.8 (75%) [9.1÷16.7] $\downarrow$	18.8 (95%) [10.0÷22.2] $\cong$	19.4 (98%) [11.8÷22.2]
Standing	<i>MAP</i> [mmHg]	95 [90÷102]	89 [95÷105] $\cong\uparrow$	87 [75÷97] $\downarrow$	70 [90÷94] $\cong\downarrow$	95 [88÷98]
	<i>SAP</i> [mmHg]	153 [136÷154]	139 [131÷151] $\cong\downarrow$	158 [127÷151] $\cong\downarrow$	110 [127÷139] $\cong\downarrow$	153 [139÷149]
	<i>DAP</i> [mmHg]	69 [72÷86]	70 [80÷90] $\cong\uparrow$	50 [57÷75] $\downarrow$	54 [73÷79] $\cong\downarrow$	69 [70÷82]
	<i>HR</i> [bpm]	79 [69÷104]	105 [82÷117] $\uparrow$	69 [60÷90] $\downarrow$	110 [80÷119] $\uparrow$	80 [73÷102]
	<i>SV</i> [ml]	62 (100%) [39÷77]	43 (69%) [28÷70] $\downarrow$	88 (142%) [41÷117] $\uparrow$	35 (57%) [85%÷109%] $\downarrow$	61 (99%) [97%÷105%]
	<i>CO</i> [l/min]	4.9 (100%) [4.3÷5.7]	4.5 (92%) [83%÷99%] $\downarrow$	6.0 (124%) [7.9÷15.1] $\uparrow$	3.9 (80%) [92%÷124%] $\downarrow$	4.9 (100%) [99%÷103%]
	<i>TPR</i> [mmHg·min/l]	19.8 (100%) [100%]	20.0 (101%) [102%÷130%] $\cong\uparrow$	14.6 (74%) [63%÷83%] $\downarrow$	17.9 (91%) [79%÷107%] $\cong$	19.8 (100%) [94%÷98%]

273 rate. The model results at 0g seated and standing posture align well with those discussed for the  
274 supine posture.

275 It is evident from Table 3 that the first and second hypergravity phases trigger the *CVS*  
276 response to a different extent. Despite keeping constant all gravity rates of variation during flight  
277 maneuvers, the drop in arterial pressure (*MAP*, *SAP* and *DAP*) is much larger for the second 1.8g  
278 phase than during the first one, with an even stronger decrease in standing (*MAP* -26% second  
279 1.8g vs. -6% first 1.8g, compared to 1g) than seated (*MAP* -13% second 1.8g vs. -1% first 1.8g,  
280 compared to 1g) posture. Meanwhile, also *SV* and *CO* fall to deeper values upon the second  
281 1.8g than during the first 1.8g phase for the standing and seated postures, with corresponding *HR*  
282 reaching higher levels (standing: +39% second 1.8g vs. +33% first 1.8g; seated: +46% second  
283 1.8g vs. +34% first 1.8g, with respect to 1g) to compensate blood pressure dip. No evident  
284 differences emerge between first and second hypergravity phases in supine posture. Among the  
285 possible reasons for such different response to 1.8 phases, one plausible factor is the different *TPR*  
286 increment promoted by short-term regulation mechanisms (in particular arterial baroreflex and  
287 cardiopulmonary reflex): the detected rise in *TPR* goes from +4% (first 1.8g) to -3% (second  
288 1.8g) for the seated posture, and from +1% (first 1.8g) to -9% (second 1.8g) for the standing  
289 posture, with respect to corresponding 1g values. The weaker *TPR* response associated with the  
290 second 1.8g phase may be due to the 20 s microgravity phase preceding the 0g-1.8g transition.  
291 During 0g, *TPR* approaches an overall vasodilated state with reduction by -25% at seated and  
292 -26% at standing posture, compared to 1g (reaching late-0g values very similar to supine 1g and  
293 0g). The fast transition from 0g to 1.8g (within 5 s) elicits a strong increment in *TPR*, whose  
294 rate of response is of the order of  $\sim 10$  s (Supplementary Table 1), but the resulting *TPR* reached  
295 after pull-out (0g-1.8g) is lower than that observed after the initial pull-up (1g-1.8g) phase, due to  
296 the different pre-transition (from 1g or 0g, respectively) *TPR* state. Therefore, the fall in blood  
297 pressure experienced during the 0g-1.8g transition is almost entirely contrasted by a further *HR*  
298 and ventricular contractility increase, both characterized by faster rate of response ( $\sim 3$  s).

## 299 4. Results

### 300 4.1. Transient response and central aortic pressure

301 Through our model, we can compute the transient behavior of several hemodynamic vari-  
302 ables over the parabolic flight maneuver, at all commonly considered postures (supine, seated and  
303 standing). In the Supplementary Material we report the transient dynamics of some meaningful  
304 hemodynamic parameters - *HR*, *CO*, *SV*, *TPR* and  $V_{cp}$ , that is cardiopulmonary compartments  
305 blood volume - during parabolic flight, and their behavior will be recalled in the following dis-  
306 cussion. Here, we focus on the transient response of central (aortic root) mean arterial pressure  
307 (*cMAP*, see Figure 3) due to its key-role in describing and understanding the overall functioning  
308 of the *CVS* when undergoing parabolic flight at different postures. Besides, *cMAP* is not typically

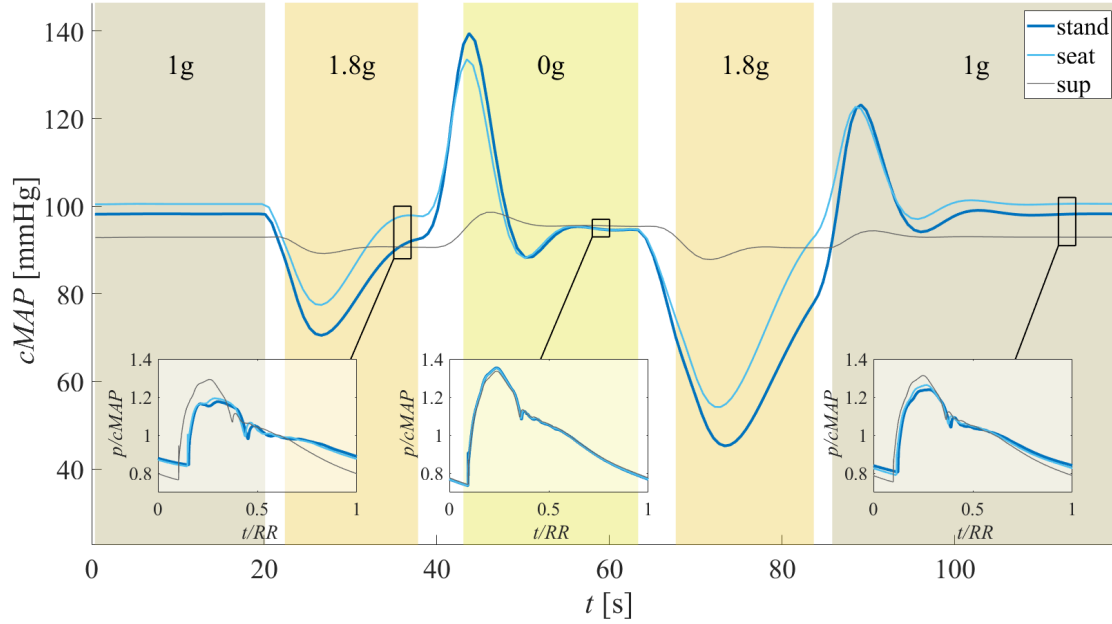


Figure 3: transient response of central (aortic root) mean arterial pressure ( $cMAP$ ) to parabolic flight at different postures (grey line: supine (sup), light blue line: seated (seat), dark blue line: standing (stand)). Snapshots of the normalized aortic root pressure waveform ( $p/cMAP$ ) - taken at each late-phase of the parabolic flight - are also reported in the insets at 1.8g, 0g and final 1g, respectively, from left to right. Normalization was performed with respect to the local heartbeat duration ( $EF$ ) and  $cMAP$ .

309 investigated during parabolic flight campaigns, because of the difficult (invasive) measurement of  
 310 such variable. Only Ogoh *et al.* [14] and Seibert *et al.* [19] reported data from continuous monitor-  
 311 ing of central aortic pressure for seated subjects during parabolic flights, although in these studies  
 312  $cMAP$  is computed through transfer function reconstruction (*e.g.*, SphygmoCor platform, AtCor  
 313 medical, or similar instruments).

314 By observing Figure 3 it is evident that the response of  $cMAP$  to parabolic flight is triggered  
 315 proportionally to the body posture (*i.e.*, stronger response in going from supine to seated and,  
 316 lastly, to standing posture). Despite the initial 1g pre-flight values of  $cMAP$  - 93 mmHg at supine,  
 317 then 98 mmHg at standing and 100 mmHg at seated posture (pressure is higher at seated than  
 318 standing because of the more effective response of short-term control in relation to a lower feetwards  
 319 blood migration) - the standing posture produces the strongest  $cMAP$  fluctuations compared to  
 320 1g pre-flight, reaching values as low as 70 mmHg (first 1.8g peak) and 45 mmHg (second 1.8g  
 321 peak). The marked reduction in  $cMAP$  registered in both 1.8g phases at seated and standing  
 322 postures is primarily due to the sudden blood migration to lower extremities, as confirmed by  
 323 the corresponding reduction in  $V_{cp}$  (Supplementary Figure 5) - reduced by about -200 ml and  
 324 -300 ml during first and second 1.8g, respectively, compared to initial 1g values, at both seated  
 325 and standing postures - and consequently in  $SV$  (Supplementary Figure 2), dropped by -20÷-30  
 326 ml at seated and standing postures with respect to 1g. As already highlighted in Table 3, the

327 model response to hypergravity at seated and standing postures produces discrepancies between  
328 computed arterial pressure and the available reference data. This holds also for *cMAP* with respect  
329 to the data reported by Ogoh et al. [14] for seated subjects, during 1.8g phases. Beside the model  
330 limitations in predicting the accurate arterial pressure response to such conditions, we should  
331 consider also the difficulties of the aortic pressure measurement performed by the authors in [14]:  
332 they did not perform a direct (*e.g.* catheterized) measurement of central aortic pressure, but the  
333 latter is obtained through transfer function reconstruction with brachial calibration, difficult to  
334 perform over a very limited time interval. During hypergravity, *HR* (Supplementary Figure 1) is  
335 raised up to 100÷110 bpm at seated and standing postures to promptly counteract the abrupt  
336 drop of *cMAP*, together with concurrent vasoconstriction of peripheral vessels (*TPR* enhanced by  
337 +10%÷+20%, see Supplementary Figure 4). As a result, during hypergravity *CO* (Supplementary  
338 Figure 3) initially drops by -22%÷-47% (first and second 1.8g negative peaks, respectively, with  
339 respect to initial 1g) at seated and standing postures, as also does *cMAP* (seated -23% and standing  
340 -29% at first early-1.8g; seated -46% and standing -54% at second early-1.8g), then both variables  
341 recover up to values slightly below (*CO*, seated -4% and standing -7% at first late-1.8g; seated -7%  
342 and standing -15% at second late-1.8g) or almost comparable (*cMAP*) to 1g pre-flight conditions.  
343 During both hypergravity phases at supine posture the *CVS* model responds in a similar way but  
344 to a much lower extent compared to seated and standing, owing to the compression of the thoracic  
345 cavity on behalf of the augmented gravity acceleration. The resulting higher *ITP* participates in  
346 disadvantaging venous return to the heart, thus weakly limiting *cMAP* (-3% at both 1.8 phases,  
347 compared to 1g), *SV* (-5 ml) and *CO* (-2%), and causing a moderate increase in *HR* (74 bpm at  
348 both 1.8g phases vs. 70 bpm at 1g).

349 The 20 s microgravity phase and the transition from previous 1.8g phase entail a number of dif-  
350 ferent responses. Given the sudden and conspicuous blood volume transfer from lower extremities  
351 to central regions ( $V_{cp}$  immediately rises by about +450 ml at seated and standing postures upon  
352 reaching 0g from 1.8g), *cMAP* is raised to almost 130÷140 mmHg, and so does *SV* (+30÷+35  
353 ml at seated and standing postures, with respect to initial 1g). Successively, following the over-  
354 all systemic relaxation with *HR* reduction to values underneath pre-flight 1g (65÷68 bpm at all  
355 postures) and peripheral vasodilation (*TPR* decreases by -37% at seated and standing postures,  
356 with respect to 1g), near pre-flight *cMAP* and *CO* supine values are approached. However, the  
357 0g *CVS* overall configuration reached in late-microgravity at all postures shows fundamental dif-  
358 ferences with respect to supine 1g pre-flight. Indeed, by complete removal of the gravity field and  
359 consequent redistribution of blood volume and pressure all over the circulation, the resulting sit-  
360 uation should be identical among postures and in turn well comparable with supine 1g pre-flight.  
361 Conversely, the *CVS* reaches a globally more relaxed configuration with respect to supine 1g,  
362 with *cMAP* little increased (95 mmHg for all postures at 0g vs. 93 mmHg at supine 1g) together  
363 with increased *SV* (about +6 ml at 0g supine posture and +10 ml at 0g seated and standing  
364 postures, compared to 1g supine) and *CO* (+2% at 0g supine posture, about +8% at 0g seated

365 and standing postures, compared to 1g supine) and reduced  $HR$  (65÷67 bpm for all postures at  
366 0g vs. 70 bpm at supine 1g) and  $TPR$  (almost no variation at 0g supine posture, about -5% at  
367 0g seated and standing postures, compared to 1g supine). The enhanced cardiac filling observed  
368 even at supine posture during microgravity (0g supine  $V_{cp}$  about +25 ml compared to 1g) is again  
369 made possible thank to the reduced  $ITP$  encountered in 0g (about -4 mmHg) compared to basal  
370 1g supine  $ITP$  (about -2.5 mmHg), allowing for reduction of  $CVP$  and therefore for promotion of  
371 cardiac preload [5, 20, 30].

372 The final 1g post-flight condition is approached after the pull-out 1.8g-1g transition phase. As  
373 for the 1.8g-0g and 0g-1.8g transitions, also the pull-up and pull-out phases show non-symmetric  
374 responses in terms of over- and undershoots of  $cMAP$  (see Figure 3) and of all other hemodynamic  
375 parameters reported in the Supplementary Material, especially at seated and standing postures.  
376 The reason for such different transient response may be linked to the lower readiness of parasym-  
377 pathetic short-term control response in regulating blood pressure compared to sympathetic activity.  
378 All variables eventually reach the same 1g pre-flight condition for all simulated postures, as also  
379 evidenced in Table 3.

380 In Figure 3 we also report the aortic root normalized pressure waveform (in the insets) referred  
381 to each late phase of flight. By analyzing the shape alteration of the aortic pressure waveform  
382 experienced at various postures and gravity accelerations, we grasp a number of aspects: (i) aortic  
383 pulse pressure - which is already reduced at 1g standing and seated postures compared to supine  
384 owing to the increased  $HR$  and diastolic pressure associated with passive orthostatic stress (refer  
385 to [21]) - undergoes further contraction with increasing gravity from 1g (right inset of Figure 3)  
386 to 1.8g (left inset) especially at seated and standing postures; (ii) entering microgravity (central  
387 inset) restores almost the same pressure waveform as in 1g supine (albeit a slight increment in  
388 pulse pressure), and no evident difference is found among postures at this stage; (iii) by looking at  
389 the temporal instants of the diastolic minimum, systolic maximum and dicrotic notch, it emerges  
390 that parabolic flight induces a marked signal phase shifting, in particular for the standing and  
391 seated posture and during hypergravity phases. Such shifting is mainly imputable to  $HR$  variation,  
392 responsible for the alteration in systolic and diastolic duration within the single heartbeat (see [21]).

#### 393 4.2. Mechano-energetic analysis

394 In Figure 4 we report the transient behaviors of the energy demand indexes  $RPP$  and  $TTI/\text{min}$   
395 and the corresponding energy supply  $SW/\text{min}$  (all indexes are presented as percentage value of  
396 their respective 1g supine conditions). We notice that  $SW/\text{min}$  at both initial 1g standing and  
397 seated postures are similar to the corresponding supine value (97% and 103% respectively), whereas  
398 oxygen demand  $RPP$  is higher than the corresponding 1g initial supine value at both seated  
399 and standing postures (110% and 112% respectively), and  $TTI/\text{min}$  is almost unchanged at all  
400 postures (except for a modest decrease at standing posture to 97% of supine 1g). Successively,  
401 as the parabolic flight maneuver is initiated reaching the first 1.8g phase,  $RPP$  rises up to 135%

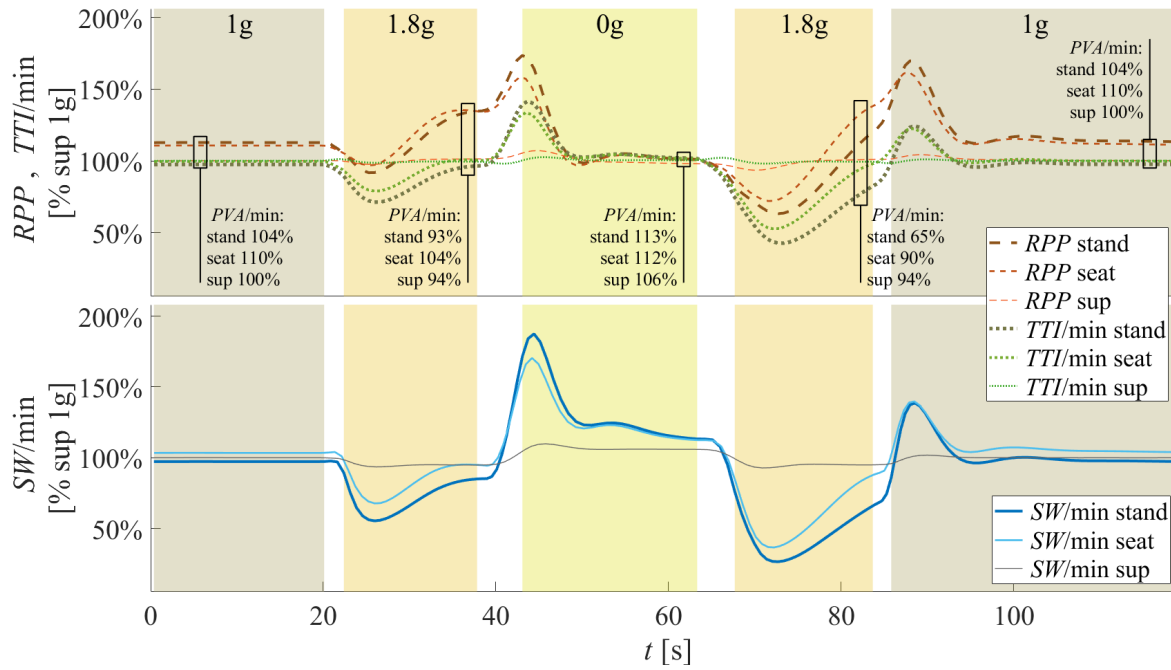


Figure 4: transient response of oxygen demand indexes (top panel)  $RPP$  (rate-pressure product: orange, dashed lines),  $TTI/min$  (tension-time index per minute: green, dotted lines) and  $PVA/min$  (pressure-volume area per minute: local values in black text) compared to left ventricle energy supply (bottom panel)  $SW/min$  (stroke work per minute: solid lines) during parabolic flight at different posture: supine, seating and standing (abbreviated as sup, mean and stand), from thin to thick lines, respectively. Percentage values as expressed with respect to corresponding supine 1g states.

402 at seated and standing postures (driven by the increasing  $HR$  and the mildly reduced  $p_{aor,sys}$ ),  
403 opposite to  $SW/min$  initially falling down to 68% (seated) and 55% (standing) - due to the  $SV$   
404 and  $V_{cp}$  drop and only partially contrasted by the increasing  $HR$  - and then recovering to about  
405 95% and 84% for the seated and standing postures, respectively. In this phase,  $TTI/min$  initially  
406 drops by -22% at seated and -29% at standing posture, compared to supine 1g, but then recovers  
407 up to 100% and 96%, respectively. Notice that, despite its late increment, percentage  $SW/min$   
408 remains lower than both  $RPP$  and  $TTI/min$  during the whole 1.8g phase, highlighting a substantial  
409 energy demand/supply unbalance. The supine posture along all the first 1.8g phase shows very  
410 weak variations, with  $SW/min$  decreased to 95% and  $RPP$  slightly augmented to 101%, while  
411  $TTI/min$  remains almost unaltered. The second 1.8g phase following 20 s microgravity exhibits a  
412 similar overall behavior, although with further pronounced undershoots - especially at seated and  
413 standing postures - due to the sudden transition from 0g to 1.8g, starting from a globally much  
414 more relaxed  $CVS$  condition (low  $HR$  and  $TPR$  at 0g).

415 The 20 s microgravity inverts the picture. After a first strong peak registered for all indexes  
416 -  $SW/min$  up to 170% at seated and 187% at standing posture,  $RPP$  to 158% at seated and  
417 172% at standing posture,  $TTI/min$  to 134% at seated and 141% at standing posture - oxygen  
418 demand indexes ( $RPP$  and  $TTI/min$ ) at all postures fall down to values below ( $RPP$ ) or prox-  
419 imal ( $TTI/min$ ) to the corresponding 1g pre-flight state, and well comparable with supine 1g  
420 pre-flight values (98%÷102% for both  $RPP$  and  $TTI/min$ ), likely because of the lowered  $HR$ .  
421 Conversely, energy supply remains at higher levels ( $SW/min$  about 114% at seated and standing  
422 postures, 106% at supine posture) in late microgravity, due to the augmented ventricular filling  
423 ( $SV$ ) promoted by the improved venous return (confirmed by the increased  $V_{cp}$  at all postures).

424 At the end of the parabolic flight maneuver, all indexes approaches the same 1g pre-flight  
425 values, even though the strong variation experienced during the pull-out phase is not perfectly  
426 symmetric with respect to the pull-up phase. Again, the reason for such behavior lies in the  
427 different response of short-term control sympathetic and parasympathetic activities in regulating  
428 blood pressure.

429 In Figure 4 we report also local percentage values of  $PVA/min$  corresponding to each late-  
430 phase of the parabolic flight. The behavior of this index of oxygen consumption is quite opposite  
431 to  $RPP$ , lying in between the corresponding local  $TTI/min$  and  $SW/min$  values. Indeed,  $PVA/min$   
432 decreases for all postures during hypergravity phases (with respect to supine 1g), whereas it rises  
433 in microgravity compared to 1g supine at all postures. The reason for such behavior can be the  
434 strong dependence of  $PVA/min$  on  $SW/min$ , explaining the similar transient response of these two  
435 parameters to the parabolic flight maneuver. However, as for  $TTI/min$ , also  $PVA/min$  exhibits  
436 reduced drops (during 1.8g phases) and rises (0g phase) compared to  $SW/min$ , confirming the  
437 above mentioned energy demand-supply unbalance.

438 Figure 5 illustrates the transient response to parabolic flight at different postures of the indexes  
439 of cardiac efficiency,  $EF$  and  $SW/PVA$ . The behavior of these two indexes is qualitatively very

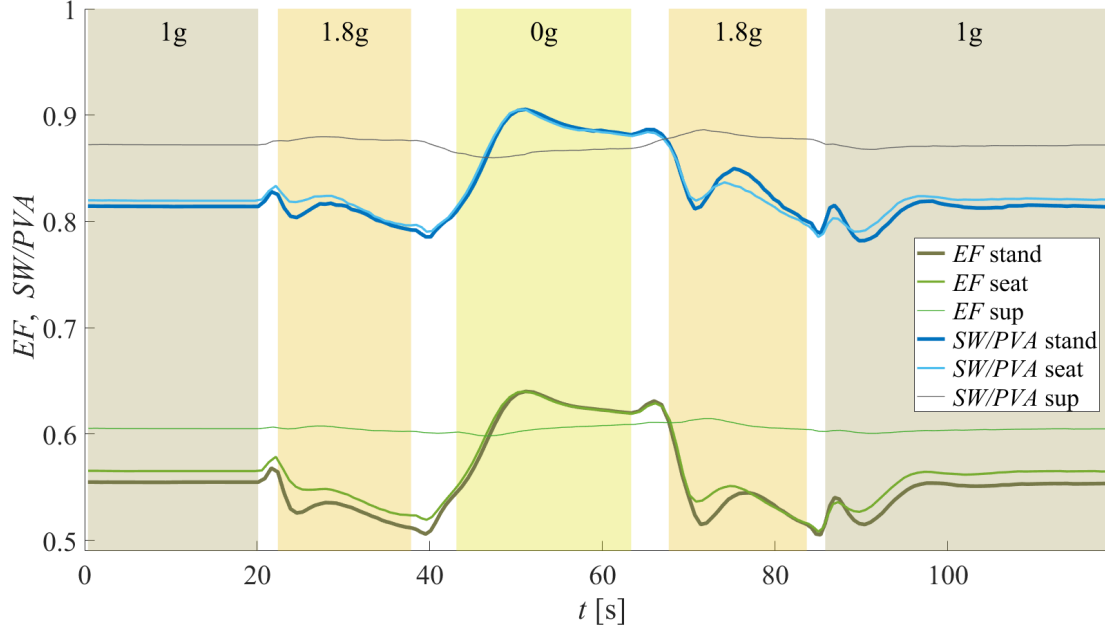


Figure 5: transient response of ventricular efficiency indexes  $EF$  (ejection fraction: lower lines) and  $SW/PVA$  (upper lines) during parabolic flight at supine, seated and standing postures (sup, seat and stand, from thin to thick lines, respectively).

440 similar, but the information carried is two-fold.  $EF$  represents the emptying performance of the  
 441 heart, that is how much the left ventricle succeeds in ejecting blood during systole. On the other  
 442 hand,  $SW/PVA$  is an index of the cardiac energy demand-supply ratio. Both indexes drop during  
 443 first hypergravity at seated and standing postures, because of the strong reduction in  $SV$  and  
 444  $SW/min$  (Figure 4). An analog response of  $EF$  and  $SW/PVA$  is encountered during the second  
 445 1.8g phase. The reduction of  $SW/PVA$  experienced during both hypergravity phases therefore  
 446 confirms the unbalance between cardiac oxygen demand and energy supply, due to the stronger  
 447 reduction of  $SW/min$  compared to  $PVA/min$  (Figure 4). Weak variations are detected for  $EF$   
 448 and  $SW/PVA$  at supine posture. In microgravity both indexes are markedly enhanced at seated  
 449 and standing postures, due to the improved  $SV$  and  $SW$  driven by the increased blood migration  
 450 from lower extremities towards central regions. Thus, in 0g the energy demand-supply unbalance  
 451 is inverted with  $SW/min$  rising more than  $PVA/min$  (Figure 4). At supine posture the behavior  
 452 of  $EF$  and  $SW/PVA$  is very weakly affected during microgravity.

453 In addition, the cardiac energy supply vs. demand balance is assessed also through the ratio  
 454 between the areas underlying the diastolic and systolic portions of the aortic pressure waveform  
 455 (shown in Figure 3), respectively, as suggested in [36]. Results, computed at each late-phase of  
 456 the parabolic flight, are reported in Table 4. At standing posture, the diastolic-to-systolic area  
 457 ratio decreases with increasing gravity (1.8g phases), confirming the previously discussed energy  
 458 demand-supply unbalance; conversely, the ratio recovers to near-supine values in 0g. The picture

Table 4: ratio between areas underlying the diastolic ( $A_{dia}$ ) and systolic ( $A_{sys}$ ) portions of the aortic pressure waveform, evaluated during each late-phase of flight. In parenthesis, the percentage values referred to supine 1g state are reported.

Aortic pressure waveform diastolic-to systolic $A_{dia}/A_{sys}$					
	1g	1.8g	0g	1.8g	1g
supine	1.49 (100%)	1.45 (97%)	1.48 (99%)	1.48 (99%)	1.49 (100%)
seated	1.47 (99%)	1.19 (80%)	1.46 (98%)	1.10 (74%)	1.47 (99%)
standing	1.41 (95%)	1.10 (74%)	1.49 (100%)	1.05 (70%)	1.40 (94%)

459 is similar at seated posture, while very weak changes with varying gravity occur at supine posture.  
 460 Unlike  $SW$  and  $SW/PVA$ , in 0g the diastolic-to-systolic area ratio does not exceed the 1g supine  
 461 value, probably because the improved diastolic duration within the heartbeat with respect to the  
 462 systolic one is compensated by the augmented systolic pressure encountered in reduced gravity  
 463 (refer to the insets in Figure 3).

## 464 5. Discussion and Conclusions

465 In this work, we used our recently developed mathematical model [21] to study the  $CVS$   
 466 behavior during a typical parabolic flight profile focusing on the role of different postures. We found  
 467 that both hyper- and microgravity elicit a number of cardiovascular responses mainly dictated  
 468 by blood volume redistribution and short-term control activation. The largest hemodynamic  
 469 alterations - in terms of aortic  $MAP$ ,  $HR$ ,  $SV$ ,  $CO$ ,  $TPR$  and  $V_{cp}$  - are registered at standing and  
 470 seated postures, although also at supine posture some minor changes are evidenced due to the  
 471 compression or relaxation of the thoracic cavity under the effect of varying gravity acceleration.  
 472 Blood redistribution from central to lower regions of the body during 1.8g phases - and *vice versa*  
 473 from lower to central regions during the 0g phase - entail prompt central pressure variation both at  
 474 aortic and carotid sinus level (involved in baroreflex control), as well as cardiac pressures variation,  
 475 including right atrial pressure (sensed by cardiopulmonary receptors). These changes trigger a  
 476 number of system responses ranging from fast improved or decreased chronotropic and inotropic  
 477 cardiac effects to successive peripheral vasoconstriction/dilation and venous tone regulation, to  
 478 cope with 1.8g and 0g conditions, respectively. Consequently,  $cMAP$  is restored to near-baseline  
 479 values in all late-phases of flight (late-1.8g, late-0g) after the strong initial fluctuations following  
 480 fast gravity transitions, with the system approaching a new configuration pertaining to each phase  
 481 of flight (in terms of  $HR$ ,  $SV$ ,  $CO$ ,  $TPR$ ,  $V_{cp}$ ).

482 In addition, we focused onto the cardiac oxygen demand-supply balance during the parabolic  
 483 flight maneuver, and we found that the mechano-energetic impairment between oxygen demand  
 484 and supply - already present at 1g seated and standing postures comparing  $RPP$  and  $SW/min$   
 485 - is further exacerbated throughout hypergravity phases at seated and standing postures. On

486 the contrary, this energy demand-supply unbalance is inverted (with  $SW/\text{min}$  overcoming  $RPP$   
487 and  $TTI/\text{min}$ ) after entering microgravity at seated and standing postures, due to the improved  
488 cardiac blood filling (and thus left ventricle  $SV$ ) and reduced ventricular rate. These findings at  
489 seated and standing postures are further corroborated by the corresponding behavior of ventricular  
490 efficiency indexes, *i.e.*,  $EF$  and  $SW/PVA$ , and by the assessment of the diastolic-to-systolic area  
491 ratio of the aortic pressure waveform. On the contrary, no evident variation of oxygen demand-  
492 supply balance emerges in supine posture throughout the parabolic flight.

493 Coherently with the observations conducted in actual spaceflight [1–5], our model describes the  
494 size of the heart as markedly increased during early-microgravity: up to +20% in cardiac volume  
495 was reported at flight day 1, well reproduced by the model predicting +8%, +15% and +23% in  
496 cardiac chambers overall volume during late-0g of parabolic flight at supine, seated and standing  
497 postures, respectively. This volume then decreases as the permanence in microgravity continues,  
498 along with spontaneous fluid loss (-15% at flight day 7), leading to cardiac atrophy in the absence  
499 of adequate countermeasures.

500 Beside the model capability of describing the global hemodynamic response to parabolic flight,  
501 a major advantage of this numerical tool is that of inquiring into the transient behavior of numer-  
502 ous poorly observed variables, due to their difficult and invasive measurement, though of great  
503 importance for some peculiar vascular regions (*e.g.*, ocular areas). As an example, we explored the  
504 plausible role of  $ICP$  in the microgravity-induced mechanisms leading to the occurrence of serious  
505 visual impairment, which may eventually lead to permanent visual acuities and morphological  
506 ocular changes [2, 5, 37, 38]. NASA has recently synthesized these symptoms as the Spaceflight-  
507 Associated Neuro-ocular Syndrome ( $SANS$ ), claiming that  $SANS$  will represent the “top health  
508 risk for long-duration spaceflight” [38]. Despite the exact etiology and pathophysiology underly-  
509 ing  $SANS$  is still unclear and widely under debate, several authors believe that  $ICP$  may play a  
510 crucial role [2, 5, 37, 38]. Recent studies conducted aboard of parabolic flights [37, 38] has shown  
511 that  $ICP$  approaches values similar to 1g supine conditions upon entering 0g ( $13 \pm 2.6$  mmHg).  
512 In light of this, researchers have hypothesized that the chronic mildly elevated  $ICP$  which the  
513 eye is subjected to during prolonged 0g can *per se* represent a potential risk factor for  $SANS$   
514 insurgence. We recall that on Earth, due to the normal circadian rhythm,  $ICP$  changes daily from  
515 slightly negative values at standing posture to  $\sim 12$  mmHg when lying supine (according to [39]  
516 the physiological range is 5-15 mmHg; Holmlund *et al.* 2017 [40] suggested a supine  $ICP$  of 10  
517 mmHg, while Lawley *et al.* 2017 [38] proposed a supine  $ICP$  of about 16 mmHg).

518 In this context, our model has already shown good capability of predicting  $ICP$  variations  
519 following change of posture [21], by embedding the  $ICP$  vs. posture relationship proposed by  
520 Holmlund *et al.* [40] (Appendix A). In the present study, the  $ICP$  behavior during parabolic flight  
521 at different postures (*i.e.*, supine, seated and standing) is examined. Figure 6 depicts punctual  
522 values of  $CVP$  (main determinant of  $ICP$ , according to [40]) and  $ICP$  at all postures referred to  
523 each late-phase of flight. We found that during both hypergravity phases  $CVP$  and  $ICP$  fall even

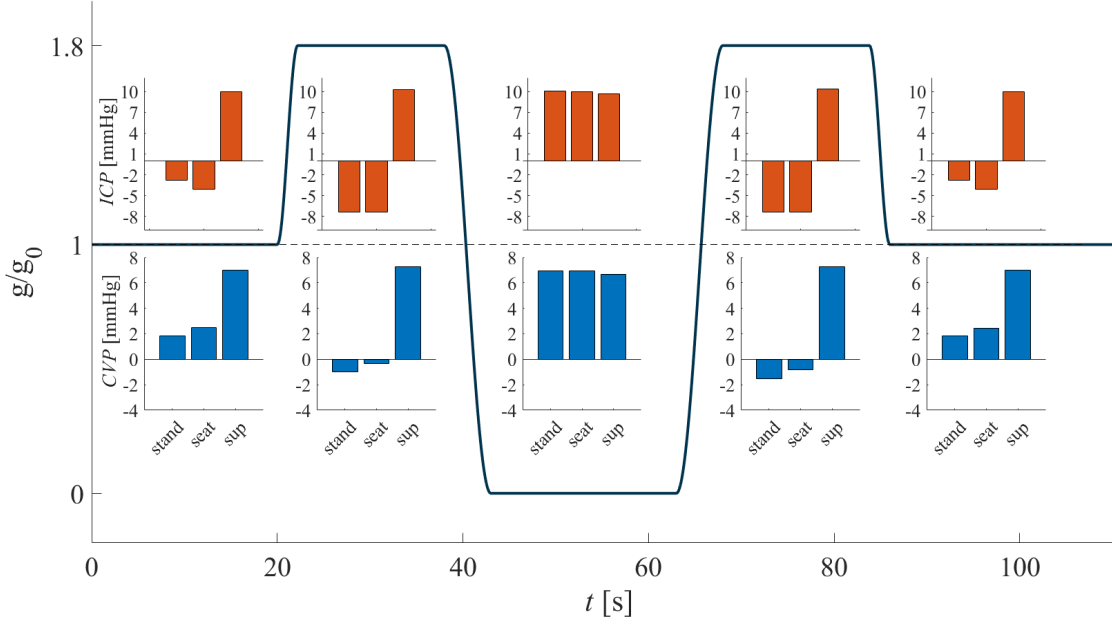


Figure 6: punctual late-phase values of central venous pressure (*CVP*, blue bars) and intracranial pressure (*ICP*, orange bars) during parabolic flight at different postures: standing, seated and supine (abbreviated as stand, seat and sup, respectively) from left to right in the bar charts.

524 more at standing and seated postures with respect to 1g (since *ITP* drops from -6.5 mmHg to -7.2  
525 mmHg), while supine values do not change significantly. Upon approaching late-0g, *CVP* and *ICP*  
526 reaches similar values for all postures, which are in turn slightly below the corresponding 1g supine  
527 values - *CVP*: 6.6 mmHg at supine 0g vs. 7 mmHg at supine 1g; *ICP*: 9.6 mmHg at supine 0g vs.  
528 10 mmHg at supine 1g - in line with data reported by Lawley *et al.* [38]. Therefore, our model  
529 confirms the mildly-elevated levels of *ICP* (though not to a pathological extent) encountered in  
530 microgravity at all postures. As believed by researchers, the prolonged maintenance of such levels  
531 of *ICP* during long-term missions may contribute to the occurrence detrimental consequences for  
532 the ocular apparatus, albeit further investigation is needed on this aspect. The implementation  
533 of a model for intraocular pressure (*IOP*) response to change of posture and gravity acceleration  
534 - including the *IOP-ICP* interplay (translaminal pressure) in determining ocular morphological  
535 changes - is needed to provide further insights into *SANS* insurgence in microgravity.

536 In conclusion, the present model lacks of muscular intervention mechanisms, which may play  
537 a role in enhancing blood pumping from lower extremities especially during hypergravity phases,  
538 where complete absence of muscular contraction cannot be excluded during *in vivo* measurements.  
539 Also, additional non-linear mechanisms as well as metabolic regulation of blood pressure and flow  
540 possibly involved in such a stressing condition (1.8g) were not considered in this study. Never-  
541 theless, the model showed good capability of reproducing known global hemodynamics response  
542 to parabolic flight at different postures, and can represent a powerful tool of investigation for

543 hemodynamic variables poorly observed in short-term microgravity owing to their difficult - and  
544 often invasive - measurement. Moreover, the analysis of cardiac energy demand-supply param-  
545 eters during parabolic flight helped shedding light onto different mechanisms affecting central  
546 and global hemodynamics upon entering short-term hyper- and microgravity environments. The  
547 model therefore reveals promising potentialities for future aerospace applications, ranging from  
548 short-term microgravity exposure to a better implementation of in-flight countermeasures.

## 549 **Competing Interests**

550 The authors declare that the research was conducted in the absence of any commercial or  
551 financial relationships that could be construed as a potential conflict of interest.

## 552 **Author Contributions**

553 All authors conceived and designed the research. M.F. performed the numerical simulations,  
554 drafted the manuscript and prepared the figures. All authors analyzed and interpreted the results,  
555 edited, reviewed and approved the final version of the manuscript.

## 556 **Supplementary Material**

557 In the online Supplementary Material, detailed model's equations and parameter definitions  
558 are provided. In addition, Supplementary Table 1 reports baroreflex and cardiopulmonary reflex  
559 modeling parameters, while Supplementary Figure 1-5 illustrate the time response of additional  
560 hemodynamic variables ( $HR$ ,  $SV$ ,  $CO$ ,  $TPR$ ,  $V_{cp}$ ) to parabolic flight at different postures.

## 561 **Data Availability Statement**

562 The raw data supporting the conclusions of this article will be made available by the authors  
563 upon request, without undue reservation.

## 564 **Appendix A.**

565 At supine posture,  $ICP$  is taken as large as 10 mmHg. As proposed in [40], by taking the  
566 difference between Davson's equation for tilted and supine posture, the relation governing  $ICP$   
567 with body posture is obtained:

$$ICP_{tilt} = ICP_{sup} + CVP_{tilt} - CVP_{sup} - \Delta p_{H-ra}^h, \quad (A.1)$$

568 where  $\Delta p_{H-ra}^h$  is the head-right atrium hydrostatic pressure difference, determined according to  
569 Stevino's law as  $\Delta p_{H-ra}^h = \rho g \Delta h_{H-ra} \sin \alpha$ , with  $\Delta h_{H-ra}$  the vertical anatomical distance between  
570 the head and the right atrium, while  $\alpha$  is the tilt angle.

571 To account for jugular vein collapsibility, only the gravity gradient associated with the fluid  
572 column extending from the head to the jugular vein point of collapse at zero transmural pressure  
573 - that is  $\Delta h_{H-jv}$  - is considered (here represented simply by  $\Delta h_H$ , assuming the jugular vein as  
574 corresponding to the superior vena cava compartment). The new relation implemented for tilt  
575 angles  $\alpha \geq \alpha_{collapse}$  reads

$$ICP_{tilt} = ICP_{sup} - CVP_{sup} - \Delta p_{H-jv}^h, \quad (A.2)$$

576 where  $\alpha_{collapse}$  is the angle for which superior vena cava pressure  $p_{svc} \leq 0$ . Intracranial pressure  
577 has been introduced only for cerebral veins. More detailed information about the cerebrovascular  
578 system model are provided in our previous work [21].

## 579 Nomenclature

580	$\alpha$	Tilt angle
581	$\rho$	Blood density
582	$\widehat{EI}$	Carotids flexural rigidity
583	$\Delta h_{H-jv}$	Head-jugular vein anatomical distance
584	$\Delta h_{H-ra}$	Head-right vertical anatomical distance
585	$\Delta p_{H-jv}^h$	Head-jugular vein hydrostatic pressure difference
586	$\Delta p_{H-ra}^h$	Head-right atrium hydrostatic pressure difference
587	$A$	Vessels cross-section area
588	$A_b$	Carotids buckling cross-section area
589	$A_{dia}$	Diastolic portion of the aortic pressure waveform area
590	$A_{sys}$	Systolic portion of the aortic pressure waveform area
591	$B_i$	Vessels mechanical coefficients
592	$cMAP$	Central arterial pressure (aorta)
593	$CO$	Cardiac output
594	$CVP$	Central venous pressure
595	$CVP_{sup}$	Central venous pressure at supine posture
596	$CVP_{tilt}$	Central venous pressure at tilted posture
597	$CVS$	Cardiovascular system
598	$C$	Vessels compliance
599	$DAP$	Diastolic arterial pressure (peripheral)
600	$EF$	Ejection fraction
601	$g_0$	Baseline (Earth) gravity acceleration
602	$g$	Gravity acceleration
603	$HR$	Heart rate
604	$ICP$	Intracranial pressure
605	$ICP_{sup}$	Intracranial pressure at supine posture

606	$ICP_{tilt}$	Intracranial pressure at tilted posture
607	$IMP$	Intramyocardial pressure
608	$IOP$	Intraocular pressure
609	$ITP$	Intrathoracic pressure
610	$la$	Left atrium
611	$lv$	Left ventricle
612	$L$	Blood inertia or inertance
613	$MAP$	Mean arterial pressure (peripheral)
614	$n$	degree of curvature of the carotid $p - A$ hyperbolic relationship
615	$pa$	Pulmonary arteries
616	$PE$	Left ventricle potential energy
617	$PVA/min$	Pressure-volume area per minute
618	$PVA$	Pressure-volume area
619	$pv$	Pulmonary veins
620	$p$	Blood pressure
621	$p_b$	Carotids buckling pressure
622	$p_{lved}$	Left ventricle end-diastolic pressure
623	$p_{lves}$	Left ventricle end-systolic pressure
624	$Q$	Blood flow rate
625	$ra$	Right atrium
626	$RPP$	Rate-pressure product
627	$RR$	Heartbeat duration
628	$rv$	Right ventricle
629	$R$	Vessels hydraulic resistance
630	$SANS$	Spaceflight-associated neuro-ocular syndrome
631	$SAP$	Systolic arterial pressure (peripheral)
632	$SV$	Stroke volume
633	$SW/min$	Stroke work per minute
634	$SW$	Stroke work
635	$TPR$	Total peripheral resistance
636	$TTI/min$	Tension-time index per minute
637	$TTI$	Tension-time index
638	$t$	Time
639	$V$	Blood volume
640	$V_{lv}^{un}$	Left ventricle unstressed volume
641	$V_{cp}$	Cardiopulmonary blood volume
642	$V_{lved}$	Left ventricle end-diastolic volume
643	$V_{lves}$	Left ventricle end-systolic volume
644	$x$	Vessels axial coordinate

645 **References**

- 646 [1] G. Clément, Fundamentals of space medicine, Vol. 23, Springer Science & Business Media,  
647 2011. doi:10.1007/978-1-4419-9905-4.
- 648 [2] L. R. Young, J. P. Sutton, Handbook of Bioastronautics, Springer, 2021. doi:10.1007/  
649 978-3-319-12191-8.
- 650 [3] H.-C. Gunga, V. W. von Ahlefeld, H.-J. A. Coriolano, A. Werner, U. Hoffmann, Cardio-  
651 vascular system, red blood cells, and oxygen transport in microgravity, Springer, 2016.  
652 doi:10.1007/978-3-319-33226-0.
- 653 [4] P. Norsk, A. Asmar, M. Damgaard, N. J. Christensen, Fluid shifts, vasodilatation and ambu-  
654 latory blood pressure reduction during long duration spaceflight, The Journal of physiology  
655 593 (3) (2015) 573–584. doi:10.1113/jphysiol.2014.284869.
- 656 [5] P. Norsk, Adaptation of the cardiovascular system to weightlessness: surprises, paradoxes  
657 and implications for deep space missions, Acta Physiologica 228 (3) (2020) e13434. doi:  
658 10.1111/apha.13434.
- 659 [6] C. N. Mukai, C. M. Lathers, J. B. Charles, B. S. Bennett, M. Igarashi, S. Patel, Acute  
660 hemodynamic responses to weightlessness during parabolic flight, The Journal of Clinical  
661 Pharmacology 31 (10) (1991) 993–1000. doi:10.1002/j.1552-4604.1991.tb03662.x.
- 662 [7] N.-Y. Bimpong-Buta, J. M. Muessig, T. Knost, M. Masyuk, S. Binneboessel, A. M. Nia,  
663 M. Kelm, C. Jung, Comprehensive analysis of macrocirculation and microcirculation in mi-  
664 crogravity during parabolic flights, Frontiers in Physiology (2020) 960doi:10.3389/fphys.  
665 2020.00960.
- 666 [8] L. G. Petersen, M. Damgaard, J. C. Petersen, P. Norsk, Mechanisms of increase in cardiac  
667 output during acute weightlessness in humans, Journal of applied physiology 111 (2) (2011)  
668 407–411. doi:10.1152/japplphysiol.01188.2010.
- 669 [9] E. G. Caiani, L. Weinert, R. Lang, P. Vaida, The role of echocardiography in the assessment  
670 of cardiac function in weightlessness—our experience during parabolic flights, Respiratory  
671 physiology & neurobiology 169 (2009) S6–S9. doi:10.1016/j.resp.2009.07.007.
- 672 [10] F. Beckers, B. Seps, D. Ramaekers, B. Verheyden, A. Aubert, Parasympathetic heart rate  
673 modulation during parabolic flights, European journal of applied physiology 90 (1) (2003)  
674 83–91. doi:10.1007/s00421-003-0854-y.
- 675 [11] U. Limper, P. Gauger, L. E. Beck, Upright cardiac output measurements in the transition to  
676 weightlessness during parabolic flights, Aviation, space, and environmental medicine 82 (4)  
677 (2011) 448–454. doi:10.3357/ASEM.2883.2011.

- 678 [12] J. Liu, B. Verheyden, F. Beckers, A. E. Aubert, Haemodynamic adaptation during sudden  
679 gravity transitions, *European journal of applied physiology* 112 (1) (2012) 79–89. doi:10.  
680 1007/s00421-011-1956-6.
- 681 [13] B. Pump, R. Videbæk, A. Gabrielsen, P. Norsk, Arterial pressure in humans during weight-  
682 lessness induced by parabolic flights, *Journal of Applied Physiology* 87 (3) (1999) 928–932.  
683 doi:10.1152/jappl.1999.87.3.928.
- 684 [14] S. Ogoh, A. Hirasawa, P. B. Raven, T. Rebuffat, P. Denise, R. Lericollais, J. Sugawara,  
685 H. Normand, Effect of an acute increase in central blood volume on cerebral hemodynamics,  
686 *American Journal of Physiology-Regulatory, Integrative and Comparative Physiology* 309 (8)  
687 (2015) R902–R911. doi:10.1152/ajpregu.00137.2015.
- 688 [15] T. T. Schlegel, T. E. Brown, S. J. Wood, E. W. Benavides, R. L. Bondar, F. Stein,  
689 P. Moradshahi, D. L. Harm, J. M. Fritsch-Yelle, P. A. Low, Orthostatic intolerance and  
690 motion sickness after parabolic flight, *Journal of applied physiology* 90 (1) (2001) 67–82.  
691 doi:10.1152/jappl.2001.90.1.67.
- 692 [16] T. T. Schlegel, E. W. Benavides, D. C. Barker, T. E. Brown, D. L. Harm, S. J. DeSilva,  
693 P. A. Low, Cardiovascular and valsalva responses during parabolic flight, *Journal of applied*  
694 *physiology* 85 (5) (1998) 1957–1965. doi:10.1152/jappl.1998.85.5.1957.
- 695 [17] D. Widjaja, S. Vandeput, S. Van Huffel, A. E. Aubert, Cardiovascular autonomic adaptation  
696 in lunar and martian gravity during parabolic flight, *European Journal of Applied Physiology*  
697 115 (6) (2015) 1205–1218. doi:10.1007/s00421-015-3118-8.
- 698 [18] P. Beck, J. Tank, P. Gauger, L. E. Beck, H. Zirngibl, J. Jordan, U. Limper, Modeling human  
699 orthostatic responses on the moon and on mars, *Clinical Autonomic Research* 28 (3) (2018)  
700 325–332. doi:10.1007/s10286-018-0527-x.
- 701 [19] F. S. Seibert, F. Bernhard, U. Stervbo, S. Vairavanathan, F. Bauer, B. Rohn, N. Pagonas,  
702 N. Babel, J. Jankowski, T. H. Westhoff, The effect of microgravity on central aortic blood  
703 pressure, *American journal of hypertension* 31 (11) (2018) 1183–1189. doi:10.1093/ajh/  
704 hpy119.
- 705 [20] R. Videbaek, P. Norsk, Atrial distension in humans during microgravity induced by parabolic  
706 flights, *Journal of Applied Physiology* 83 (6) (1997) 1862–1866. doi:10.1152/jappl.1997.  
707 83.6.1862.
- 708 [21] M. Fois, S. V. Maule, M. Giudici, M. Valente, L. Ridolfi, S. Scarsoglio, Cardiovascular response  
709 to posture changes: Multiscale modeling and in vivo validation during head-up tilt, *Frontiers*  
710 *in Physiology* 13 (2022). doi:10.3389/fphys.2022.826989.

- 711 [22] A. D. Artiles, T. Heldt, L. R. Young, Effects of artificial gravity on the cardiovascular sys-  
712 tem: computational approach, *Acta Astronautica* 126 (2016) 395–410. doi:10.1016/j.  
713 actaastro.2016.05.005.
- 714 [23] R. S. Whittle, A. Diaz-Artiles, Modeling individual differences in cardiovascular response to  
715 gravitational stress using a sensitivity analysis, *Journal of Applied Physiology* 130 (6) (2021)  
716 1983–2001. doi:10.1152/jappphysiol.00727.2020.
- 717 [24] C. Gallo, L. Ridolfi, S. Scarsoglio, Cardiovascular deconditioning during long-term space-  
718 flight through multiscale modeling, *npj Microgravity* 6 (1) (2020) 1–14. doi:10.1038/  
719 s41526-020-00117-5.
- 720 [25] B. Gerber, J.-L. Singh, Y. Zhang, W. Liou, A computer simulation of short-term adaptations  
721 of cardiovascular hemodynamics in microgravity, *Computers in Biology and Medicine* 102  
722 (2018) 86–94. doi:10.1016/j.compbimed.2018.09.014.
- 723 [26] G. Drzewiecki, S. Field, I. Moubarak, J. K.-J. Li, Vessel growth and collapsible pressure-  
724 area relationship, *American Journal of Physiology-Heart and Circulatory Physiology* 273 (4)  
725 (1997) H2030–H2043. doi:10.1152/ajpheart.1997.273.4.H2030.
- 726 [27] K. i. Iwasaki, Y. Ogawa, K. Aoki, R. Yanagida, Cerebral circulation during mild+ gz hyper-  
727 gravity by short-arm human centrifuge, *Journal of applied physiology* 112 (2) (2012) 266–271.  
728 doi:10.1152/jappphysiol.01232.2011.
- 729 [28] C. Leguy, P. Beck, P. Gauger, L. Beck, U. Limper, Carotid arterial wall dynamics during  
730 gravity changes on partial-g parabolic flights, *Microgravity Science and Technology* 26 (2)  
731 (2014) 111–117. doi:10.1007/s12217-014-9381-1.
- 732 [29] D. Linnarsson, C. Sundberg, B. Tedner, Y. Haruna, J. Karemaker, G. Antonutto, P. Di Pram-  
733 pero, Blood pressure and heart rate responses to sudden changes of gravity during exercise,  
734 *American Journal of Physiology-Heart and Circulatory Physiology* 270 (6) (1996) H2132–  
735 H2142. doi:10.1152/ajpheart.1996.270.6.H2132.
- 736 [30] K. Peterson, E. T. Ozawa, G. M. Pantalos, M. K. Sharp, Numerical simulation of the influence  
737 of gravity and posture on cardiac performance, *Annals of biomedical engineering* 30 (2) (2002)  
738 247–259. doi:10.1114/1.1451075.
- 739 [31] A. Guala, C. Camporeale, F. Tosello, C. Canuto, L. Ridolfi, Modelling and subject-specific  
740 validation of the heart-arterial tree system, *Annals of biomedical engineering* 43 (1) (2015)  
741 222–237. doi:10.1007/s10439-014-1163-9.

- 742 [32] F. Melchior, R. Srinivasan, P. Thullier, J. Clere, Simulation of cardiovascular response to  
743 lower body negative pressure from 0 to-40 mmhg, *Journal of Applied Physiology* 77 (2)  
744 (1994) 630–640. doi:<https://doi.org/10.1152/jappl.1994.77.2.630>.
- 745 [33] J. Mynard, J. Smolich, One-dimensional haemodynamic modeling and wave dynamics in the  
746 entire adult circulation, *Annals of biomedical engineering* 43 (6) (2015) 1443–1460. doi:  
747 <https://doi.org/10.1007/s10439-015-1313-8>.
- 748 [34] A. Saglietto, M. Fois, L. Ridolfi, G. M. De Ferrari, M. Anselmino, S. Scarsoglio, A computa-  
749 tional analysis of atrial fibrillation effects on coronary perfusion across the different myocardial  
750 layers, *Scientific reports* 12 (1) (2022) 1–9. doi:[10.1038/s41526-020-00117-5](https://doi.org/10.1038/s41526-020-00117-5).
- 751 [35] T. Klein, P. Wollseiffen, M. Sanders, J. Claassen, H. Carnahan, V. Abeln, T. Vogt, H. K.  
752 Strüder, S. Schneider, The influence of microgravity on cerebral blood flow and electro-  
753 cortical activity, *Experimental brain research* 237 (4) (2019) 1057–1062. doi:[10.1007/  
754 s00221-019-05490-6](https://doi.org/10.1007/s00221-019-05490-6).
- 755 [36] N. Westerhof, N. Stergiopoulos, M. I. Noble, B. E. Westerhof, Cardiac oxygen consumption  
756 and hemodynamics, in: *Snapshots of Hemodynamics*, Springer, (2010), pp. 129–134. doi:  
757 [10.1007/978-1-4419-6363-5](https://doi.org/10.1007/978-1-4419-6363-5).
- 758 [37] L.-F. Zhang, A. R. Hargens, Spaceflight-induced intracranial hypertension and visual im-  
759 pairment: pathophysiology and countermeasures, *Physiological reviews* 98 (1) (2018) 59–87.  
760 doi:[10.1152/physrev.00017.2016](https://doi.org/10.1152/physrev.00017.2016).
- 761 [38] J. S. Lawley, L. G. Petersen, E. J. Howden, S. Sarma, W. K. Cornwell, R. Zhang, L. A.  
762 Whitworth, M. A. Williams, B. D. Levine, Effect of gravity and microgravity on intracranial  
763 pressure, *The Journal of physiology* 595 (6) (2017) 2115–2127. doi:[10.1113/JP273557](https://doi.org/10.1113/JP273557).
- 764 [39] A. Tameem, H. Krovvidi, Cerebral physiology, *Continuing Education in Anaesthesia, Critical*  
765 *Care & Pain* 13 (4) (2013) 113–118. doi:[10.1093/bjaceaccp/mkt001](https://doi.org/10.1093/bjaceaccp/mkt001).
- 766 [40] P. Holmlund, A. Eklund, L. Koskinen, E. Johansson, N. Sundström, J. Malm, S. Qvarlander,  
767 Venous collapse regulates intracranial pressure in upright body positions, *American Journal of*  
768 *Physiology-Regulatory, Integrative and Comparative Physiology* 314 (3) (2018) R377–R385.  
769 doi:<https://doi.org/10.1152/ajpregu.00291.2017>.